

REVIEW ARTICLE

Random lasers based on organic epitaxial nanofibers

Francesco QuochiDipartimento di Fisica, Università di Cagliari, SLACS-INFM/CNR,
I-09042 Monserrato (CA), ItalyE-mail: francesco.quochi@dsf.unica.it

Received 7 July 2009, accepted for publication 6 August 2009

Published 11 January 2010

Online at stacks.iop.org/JOpt/12/024003**Abstract**

We present a review on random lasing in organic nanofibers made of oligophenyl nanocrystals grown by molecular epitaxy on polar substrates. The nanofibers have sub-wavelength cross-sectional dimensions and can extend in length up to the millimeter scale. We report on random lasing properties of nanofibers, under subpicosecond photopumping, both in the coherent and incoherent regimes. With the aid of both optical and morphological studies on individual fibers, we get insight into one-dimensional coherent feedback taking place along the nanofibers' axes. Model calculations of light propagation in disordered media allow us to give a semiquantitative description of one-dimensional coherent random lasing near the lasing threshold. We also report on amplified simulated emission in individual nanofibers and demonstrate that nanoscale linear optical amplifiers can be obtained by molecular self-assembly at surfaces. Photophysical studies of nanofibers resorting to subpicosecond luminescence and pump-probe spectroscopy give us valuable information on temperature-dependent, excited-state nonlinear processes, such as exciton-exciton annihilation and photoinduced absorption. Excited-state effects strongly influence lasing thresholds under quasi-continuous-wave photoexcitation conditions, as demonstrated in photoexcitation experiments performed with nanosecond pulses. Last, we briefly discuss the potential of organic epitaxial nanofibers featuring low-threshold random lasing for photonic sensing applications.

Keywords: molecular epitaxy, self-assembly, nanofibers, random lasing, amplified spontaneous emission, exciton-exciton annihilation, photoinduced absorption, photonic sensing

(Some figures in this article are in colour only in the electronic version)

1. Introduction

Random lasing is an active field of research from both experimental and theoretical points of view. In a random laser, optical feedback is provided by a chain of disorder-induced light scattering events inside the gain medium. Sequential scattering can result in field resonance conditions on closed-loop propagation paths or just in increase of the optical propagation path length on open-loop paths. In the former case one refers to *coherent random lasing*, while in the latter case random lasing is incoherent and feedback does not apply to the field amplitude, but just to radiant energy [1]. *Incoherent random lasing* could be exploited to turn moderate material gain coefficients into large amplification factors in optical

devices. Coherent random lasing retains the basic properties of conventional lasers, i.e., spectrally narrow emission modes, which greatly enhance the range of potential applications. In strongly scattering material systems, photon localization can occur, leading to lasing modes with spatial extension on the order of the light wavelength in the medium [2]. Recently, applications of random lasers in the strong localization regime have been envisaged in nanophotonics and remote sensing [3]. Biomedical applications of coherent random lasing in cancer diagnostics have also been proposed [4].

Organic materials based on molecular or polymer aggregates with some degree of disorder are suitable for the realization of random lasers with different dimensionalities and spatial and spectral properties. Two-dimensional organic

thin films and one-dimensional nanostructures can be realized at surfaces by different methods at relatively low cost. In addition, conjugated organics display photophysical properties that are suitable for the achievement of (random) laser devices with improved performances, such as large optical cross-sections for low-threshold operation, and high bandwidths for extended wavelength tunability [5, 6].

Solid state organic random lasers with two-dimensional coherent feedback have been successfully demonstrated in both polymer [7] and molecular [8] thin films realized by spin coating on substrates. Random lasing with one-dimensional coherent feedback has recently been achieved in organic molecular nanofibers epitaxially grown on polar substrates [9].

Other one-dimensional organic nanostructures have been demonstrated, i.e., single-crystalline molecular nanowires [10] and polymer nanowires [11, 12]. These nanostructures are synthesized by adsorbent-assisted physical vapor deposition [10], melt-assisted template wetting [11] or electrospinning followed by a nanoimprinting process [12]. All of these organic nanostructures yield lasing action on well defined resonator modes, though one can conceive of obtaining random lasing derivatives of the same nanostructures for specific applications.

It is the purpose of this paper to give a review on random lasing properties, as well as excited-state and photophysical processes, of epitaxially grown oligophenyl nanofibers. Deposition of *para*-sexiphenyl (*p*-6P) and similar oligomers on polar substrates, such as muscovite mica, leads to the self-assembly of highly anisotropic aggregates through a dipole-induced dipole surface interaction mechanism [13–15]. Needle-shaped aggregates are formed with typical lengths of tens to hundreds of micrometers and cross-sectional dimensions (widths and heights) on the order of 100 nm. Oligophenyl nanofibers feature a high degree of epitaxial alignment; the long molecular axes are nearly parallel to the substrate and perpendicular to the needles' axes [16, 17]. They also display a number of important optoelectronic properties, i.e., charge carrier mobilities ranging from $\sim 10^{-2}$ to ~ 10 cm² V⁻¹ s⁻¹, depending on the fabrication details [18, 19], strong optical anisotropy both in absorption and emission [14], light waveguiding [20, 21], Raman gain amplification [22], photoinduced spectral narrowing [23], amplified spontaneous emission (ASE) [24] and coherent random lasing [9, 16, 25, 26]. Surface contamination of the substrate can also be exploited to obtain morphologically diverse nanoaggregates, such as ring-shaped structures [27].

The paper is organized as follows. In section 2 we provide general information on fabrication and characterization of *p*-6P epitaxial nanofibers. In section 3 we describe the properties of random lasing observed in ensembles of nanofibers. In section 4 we show the results of combined optical spectroscopy and atomic force microscopy for individual nanofibers, elucidating the mechanisms at the origin of the coherent optical feedback in the nanofibers. Section 5 is devoted to individual nanofibers acting as linear optical amplifiers through ASE. In section 6 we present a comprehensive study of the excited-state dynamics of epitaxial *p*-6P films and report on random laser action under nanosecond-pulsed excitation conditions. In section 7 we discuss the potential for random lasing in

one-dimensional organic nanostructures such as *p*-6P epitaxial nanofibers for photonic sensing applications. Lastly, section 7 presents a conclusive summary of this work.

2. Growth and characterization of *p*-6P epitaxial nanofibers

Para-sexiphenyl nanofiber films are grown on freshly cleaved, (001)-oriented muscovite mica by hot-wall epitaxy (HWE) [14] and organic molecular beam deposition (OMBD) [15]. In the HWE technique, *p*-6P is purified by threefold sublimation under a dynamic vacuum. The base pressure during growth is about 6×10^{-6} mbar and the *p*-6P source temperature is fixed at 240 °C. The substrate temperature is 130 °C. The growth time is varied between 10 s and 120 min. Further details can be found in [28, 29]. In the OMBD technique, sheets of muscovite mica (SPI) are cleaved in air and are transferred immediately after cleavage into a high-vacuum apparatus (base pressure of 5×10^{-8} mbar). Before organic material is deposited, the samples are outgassed at a temperature of around 130 °C such that low-energy electron diffraction shows the well-known hexagonal surface structure of clean mica with electric surface dipoles present. *Para*-sexiphenyl is deposited from a home-built Knudsen cell by vacuum sublimation; during the deposition the pressure inside the vacuum system rises to 2×10^{-7} mbar. Long *p*-6P needles grow for deposition rates of 0.1 Å s⁻¹ and at substrate temperatures around 150 °C.

Morphological characterization of the nanofibers is performed by scanning-probe atomic force microscopy (AFM) using Si-tip probes in tapping mode in air. Complementary optical characterization is carried out by means of cw epifluorescence measurements using an inverted microscope with a Hg high-pressure lamp as the excitation source.

AFM topographic studies of the surface morphology of films prepared by HWE with increasing growth times demonstrate that nanofibers are self-assembled by regrouping of mobile individual crystallites that originate at the very early growth stages by (for deposition times <10–25 s) [16]. For growth times longer than 5 min, only linear fibers are observed. A surface topographic image of films obtained with 40 min growth time is shown in figure 1. For long deposition times, close-packed and interconnected nanofibers are realized.

Figure 2 depicts the surface morphology of a small ($\sim 5 \times 5.5$ μm²) film area displaying sparse nanofibers. Typical features of isolated nanofibers on the length scale of a few micrometers are visible. The nanofibers have a base width of 300 nm or larger and a height on the order of 100 nm, which enables waveguiding of *p*-6P fluorescence [20, 21]. The small islands lying between adjacent nanofibers are remnants of the nucleation process of *p*-6P into oriented fibers. Occurrence of material breaks, typically 50–300 nm wide, implies segmentation of the nanofibers. Such thin breaks occur possibly at the end of the material growth process as a result of a surface thermal gradient during substrate cooling [15]. Breaks characterize most nanofibers although there exist a population of break-free nanofibers in most samples. Breaks are responsible for light scattering into out-of-plane directions and back-scattering (i.e., modal reflection) of

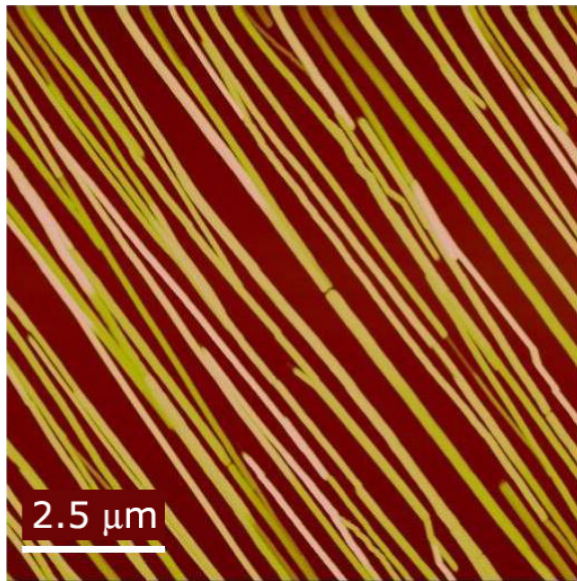


Figure 1. $10 \times 10 \mu\text{m}^2$ AFM topographic image of the surface morphology of a *p*-6P film grown by HWE on (001)-oriented muscovite mica. The growth time (t), data color scale (range), and nanofiber average base width (b) and height (h) are as follows: $t = 40$ min, range = 0–220 nm, $\langle b \rangle \approx 210$ nm, $\langle h \rangle \approx 110$ nm.

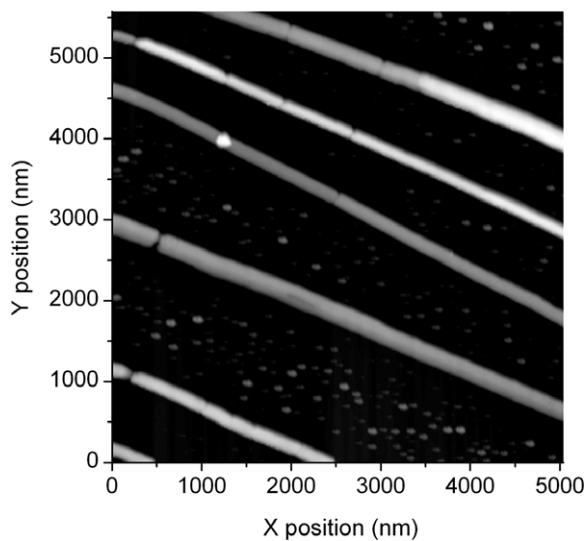


Figure 2. Grayscale AFM topographic image of the surface morphology of *p*-6P nanofibers grown on (001)-oriented muscovite mica by OMBD. The grayscale range is 0–95 nm.

the fiber waveguide modes, thereby enabling the establishing of one-dimensional coherent feedback along the nanofibers' axes (see section 4).

Epifluorescence micrographs of the nanofibers' ensembles provide valuable information on the fibers' optical quality (figure 3). The fluorescence emission profiles of individual fibers are homogeneous, except for special locations where the intensity of the emission scattered out of the substrate plane is strongly enhanced, yielding bright spots in the epifluorescence images. Fluorescence waveguiding is inferred to take place over segments ranging in length from micrometers to tens of micrometers.

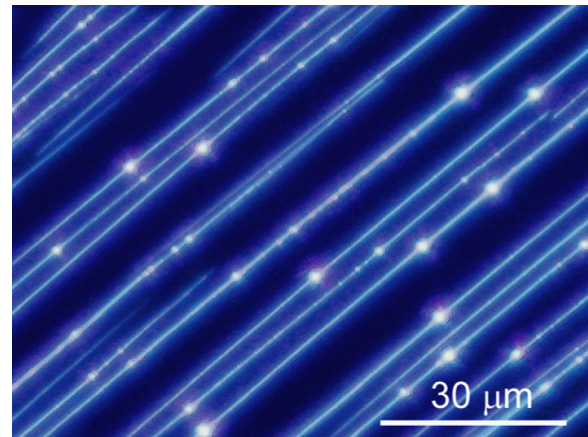


Figure 3. Cw epifluorescence micrograph of a *p*-6P film grown on (001)-oriented muscovite mica by OMBD.

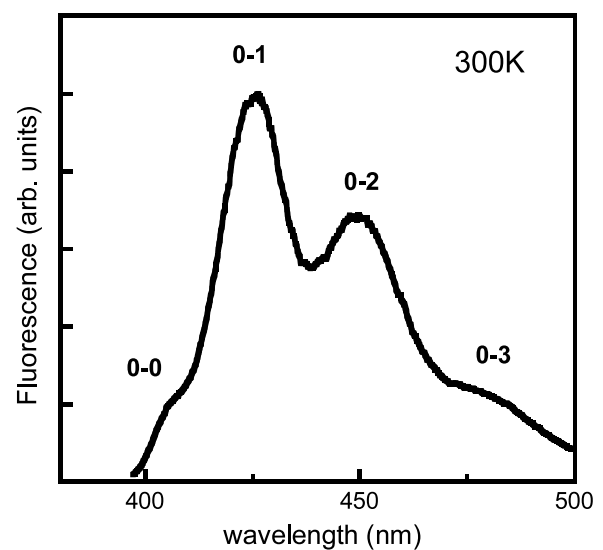


Figure 4. Room temperature epifluorescence spectrum of *p*-6P crystalline nanofibers grown on (001)-oriented muscovite mica.

Figure 4 shows the emission spectrum of *p*-6P nanofibers at room temperature. The spectrum shows the typical features of H aggregates, that is, a weak electronic (0–0) transition and a more intense vibronic progression involving the C–C stretching mode.

3. Coherent versus incoherent random lasing in *p*-6P epitaxial nanofibers

To investigate nanofiber lasing, ensembles of *p*-6P nanofibers are optically pumped using ultrashort (~ 150 fs) laser pulses of a frequency-doubled (380–390 nm) Ti:sapphire regenerative amplifier running at a repetition frequency of 1 kHz. The pump beam is focused to circular spots ranging from 120 to 180 μm in diameter on the samples, allowing us to achieve pump fluence values as high as $1 \text{ mJ cm}^{-2}/\text{pulse}$. The pump field polarization is set perpendicular to the axis of the nanofibers (and thus parallel to the long axis of the *p*-6P molecules) for maximum optical absorption. The optical emission spot is

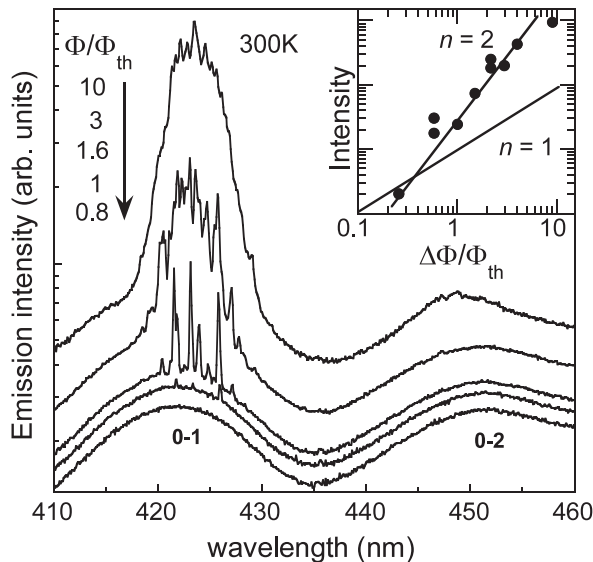


Figure 5. Ensemble-averaged optical emission spectra of close-packed *p*-6P nanofibers excited by subpicosecond pulses, for different pulse fluences given in relative units Φ/Φ_{th} , where Φ_{th} is the fluence value at the random lasing threshold. The spectra are taken at room temperature. Inset: spectrally integrated intensity of the nonlinear emission (above threshold) upon removal of the luminescence background. Power-law functions (exponent n) are represented by the solid lines.

focused onto the input slit of a single imaging spectrometer equipped with a liquid N₂ (LN₂) cooled charge-coupled device (CCD) for high-sensitivity measurements [25].

Evidence of coherent random lasing is provided in figure 5, where the sum of the emission spectrum of some tens of close-packed, interconnected nanofibers (ensemble-averaged spectrum) is reported for different values of the excitation fluence, at room temperature. At low excitation levels, only spontaneous emission is observed. When the excitation fluence exceeds threshold values (Φ_{th}) as low as $1 \mu\text{J cm}^{-2}/\text{pulse}$, resolution-limited peaks emerge from the spontaneous emission spectrum for the 0–1 vibronic band. As pump fluence is further increased the visibility of the narrow lines decreases until spectral narrowing of the vibronic peak dominates the system response. Laser-like peaks denote the presence of field resonance paths within the *p*-6P films, while spectral narrowing of the 0–1 and 0–2 emission peaks indicates that incoherent amplification (ASE) occurs at the highest pump levels. In the inset, the emission intensity is plotted as a function of the normalized pump excess fluence, defined as $\Delta\Phi/\Phi_{th} = (\Phi - \Phi_{th})/\Phi_{th}$. The signal intensity is spectrally integrated over the 0–1 band upon subtraction of the luminescence background. The nonlinear dependence of the emission intensity on $\Delta\Phi/\Phi_{th}$ is explained considering that the number of coherent modes that reach oscillation threshold increases with pump fluence and by the ASE process.

Spatial and polarization sensitivities of coherent random lasing in *p*-6P crystalline nanofibers are reported in figure 6. Figure 6(a) shows that random lasing spectrum is very sensitive to the position of the pump spot on the sample surface. The excitation of different nanofibers' ensembles results in laser oscillation of coherent modes having different resonance

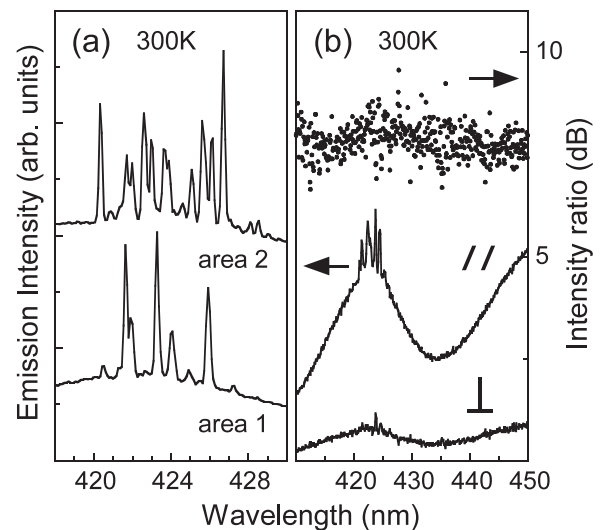


Figure 6. Ensemble-averaged emission spectra of close-packed *p*-6P nanofibers excited by subpicosecond pulses: (a) two different areas of the sample; (b) after polarization filtering along the direction parallel (//) and perpendicular (\perp) to the long molecular axis of *p*-6P. Dots: intensity ratio between the two polarization-filtered spectra. The spectra are taken at room temperature.

wavelengths and losses. This also explains why strong variation in lasing threshold fluence is registered as the excited area is changed. As expected from the film anisotropy and epitaxial alignment, both linear and nonlinear optical emission exhibit strong polarization anisotropy with intensity ratios on the order of 10 dB (figure 6(b)).

Characteristics of random lasing excited by subpicosecond pulses, shown here in room temperature measurements, are found to be weakly dependent on temperature in the 80–300 K range. The twofold or threefold increase in the random lasing threshold typically observed upon the sample cooling to 80 K is attributed to blueshift of the *p*-6P absorption bandgap, with consequent reduction of the photoexcitation density created at a fixed pump wavelength near the gap (380–390 nm). The lasing threshold fluence becomes extremely sensitive to the lattice temperature when laser action is induced by pulses whose duration is longer than the *p*-6P excited-state lifetime (see section 6).

4. One-dimensional coherent random lasing in individual *p*-6P epitaxial nanofibers

Optical studies on isolated *p*-6P nanofibers allow us to elucidate the mechanisms at the origin of the coherent optical feedback responsible for random lasing. While optical feedback realized in interconnects of close-packed nanofibers has allegedly two-dimensional character, isolated nanofibers represent a test bed for one-dimensional random lasing in organic epitaxial nanostructures.

We investigate *p*-6P films exhibiting long and isolated nanofibers by means of microspectrographic measurements with ultrafast pumping. The samples are excited at normal incidence from the back surface of the substrate. The emission is collected from the front surface using a microscope objective

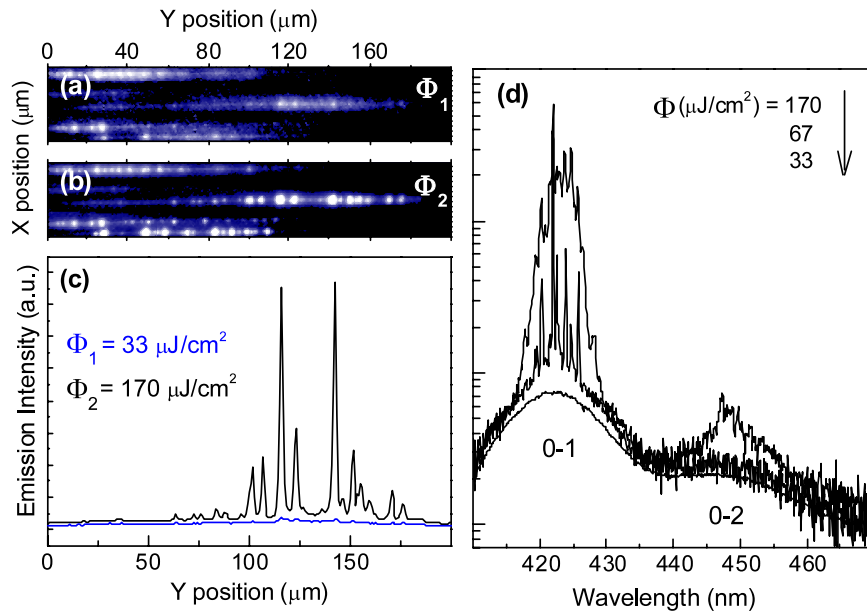


Figure 7. Time integrated emission micrographs of nanofibers excited by ultrafast pulses, for pump fluences $\Phi_1 = 33$ (a) and $\Phi_2 = 170 \mu\text{J cm}^{-2}$ /pulse (b). Panel (c): time and spectrally integrated spatial profiles of the emission intensity of the nanofiber placed at the center of the micrographs shown in panels (a) and (b). Panel (d): time integrated emission spectra of the same nanofiber for different values of the excitation fluence. Sample temperature: 300 K.

which focuses it onto the input slit of the spectrometer. Setting the spectrograph to zeroth-order diffraction and fully opening the input slit, one can image the fluorescence spot at the sample surface with $\sim 2 \mu\text{m}$ spatial resolution. Tuning the spectrometer to first-order diffraction and narrowing the input slit, the detection system becomes a microspectrometer that enables us to spectrally resolve the emission of individual nanofibers aligned parallel to the input slit [9].

Figure 7 depicts emission micrographs of isolated nanofibers taken (a) below and (b) above the lasing threshold. Lasing action produces a dramatic enhancement of the visibility of optical scattering centers. This result is clear also from figure 7(c), which displays spatial profiles of the epifluorescence emission of the nanofiber $\sim 100 \mu\text{m}$ long placed at the center of the micrographs. Spatially integrated emission spectra of the same nanofiber are reported in figure 7(d). The random lasing threshold is first reached at the 0–1 peak, and, at a slightly higher fluence, also at the 0–2 peak. As expected for a single laser emitter, spontaneous emission saturates at the value reached at threshold. Fluorescence clamping is not observed in ensemble-averaged measurements, since not all excited fibers reach the lasing threshold (figure 5).

Correlated lasing measurements and AFM topographic measurements give insight into the origin of one-dimensional coherent feedback in individual *p*-6P nanofibers. Figure 8(a) shows the AFM topographic image of a nanofiber $\sim 100 \mu\text{m}$ long. When the fiber morphology is compared to the lasing intensity profile for the same region (figures 8(b) and (c)), it turns out that scattering of the guided lasing emission occurs at the fiber breaks. In fact, excellent correspondence is found between the positions of the bright lasing spots and those of the fiber breaks. Measurements in other isolated nanofibers give very similar results. These findings strongly support the

idea that back-reflections of the fiber waveguide modes at the fiber break interfaces are the main source of optical feedback along the nanofibers' axes.

Our interpretation of the experimental data in terms of one-dimensional coherent random lasing is supported by calculations of the resonant optical modes of one-dimensionally disordered systems. Neglecting modal effects relating to lateral optical confinement, coherent light propagation is computed across a multilayered structure (made of material slabs, simulating fiber segments, separated by thin air gaps, which stand for fiber breaks) using a transfer-matrix formalism. The refractive index step between the material ($n = 1.7$) and air causes partial back-reflection of the optical field at each material–air interface. Since the theoretical spectrum varies strongly with the disorder realization, calculations are carried out using actual structural data derived from AFM topography. With reference to the nanofiber displayed in figure 8, 17 slabs of different lengths, separated by 240 nm wide air gaps, are used for the calculations. As fiber breaks are not delimited by well defined facets and thus do not possess well defined widths, the same value is used for all air gap widths. Losses caused by out-of-plane light scattering at the fiber breaks' positions are taken into account. Distributed propagation losses, such as material self-absorption, are compensated by optical gain to simulate the system response near the lasing instability [30], where the linewidth of resonant modes drops to zero.

In figure 9 we show the emission spectrum measured at the position of the fiber break labeled as 'break 2' in figure 8 and compare it to the optical intensity spectrum calculated at the same position. The calculated intensity spectrum is multiplied by a Gaussian with 14 nm width (FWHM), centered at 424 nm, to simulate the 0–1 vibronic band of the *p*-

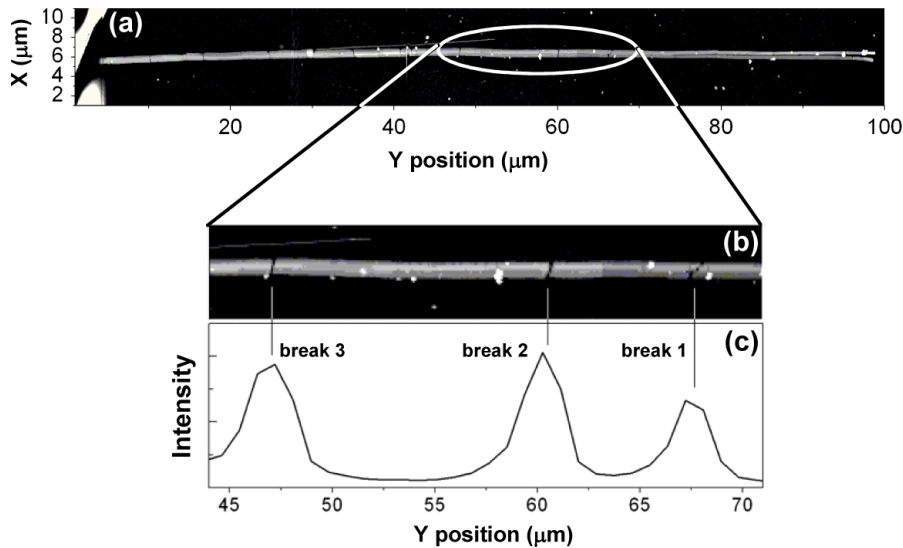


Figure 8. (a) Gray-level scale AFM topographic image of the surface morphology of a single *p*-6P nanofiber. The gray-level scale range is 0–95 nm. (b) AFM image of the same nanofiber zoomed in on a smaller region. (c) Spatial profile of the lasing emission intensity zoomed in on the same fiber region. The vertical markers placed across panels (b) and (c) demonstrate the position correspondence between bright emission spots and fiber breaks.

6P emission. Our distributed feedback model accounts well for the experimental random lasing spectra on a qualitative basis. As regards the spectral domain, the model is able to reproduce the density of lasing modes, although inclusion of modal propagation effects in the calculations turns out to be necessary for predicting resonance wavelengths and intensities in a quantitative way. The central role played by fiber breaks in realizing random resonance modes through one-dimensional multipath interference is highlighted by the results of control calculations done with decreasing air gap widths. When the width of the air gaps goes to zero, random modes disappear and the intensity spectrum tends to that of a Fabry–Perot resonator having the length of the nanofiber ($\sim 101 \mu\text{m}$), thus exhibiting spectral fringes with $\sim 0.5 \text{ nm}$ spacing (top curve in figure 9). As regards the spatial domain, since (i) out-of-plane light scattering occurs at the fiber breaks and (ii) breaks' actual positions are used in the model multilayered structure, model calculations automatically reproduce the intensity profile of the lasing emission.

5. Linear amplified spontaneous emission in individual *p*-6P epitaxial nanofibers

Determination of net modal gain in individual fibers yields the ultimate amplification performance of *p*-6P crystalline nanofiber waveguides. With this purpose, we select homogeneous, break-free nanofibers, in which retrieval of net gain is not hindered by random laser action [24], and apply the same microspectrographic technique as was used to characterize coherent random lasing in segmented fibers.

Typical results are reported in figure 10. At low excitation levels, the emission micrograph of a selected nanofiber shows the absence of scattering centers in between the fiber tips (figure 10(a)). Increasing the pump fluence above a threshold value of $\sim 100 \mu\text{J cm}^{-2}/\text{pulse}$, enhancement of the emission

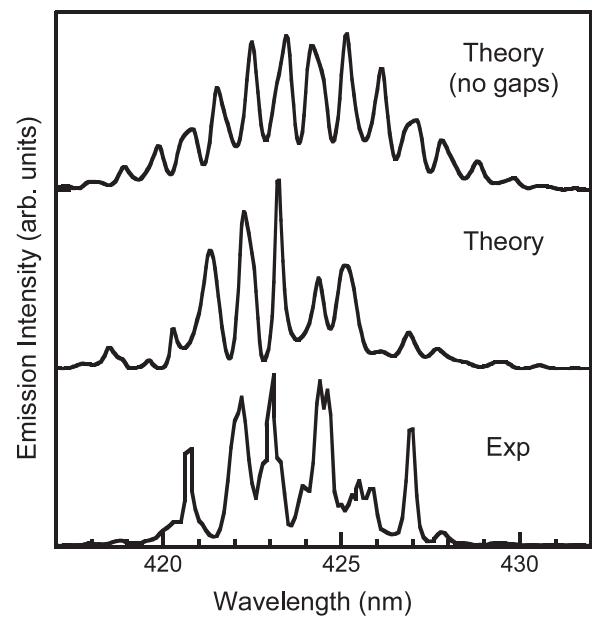


Figure 9. ‘Exp’: random lasing spectrum of a single *p*-6P nanofiber probed at the position of a fiber break. The pump fluence is just above the lasing threshold. ‘Theory’: the corresponding coherent field intensity spectrum calculated on the basis of a transfer-matrix model, using fiber morphological parameters extracted from AFM topography. ‘Theory no gaps’: the intensity spectrum calculated upon setting the width of the air gaps equal to zero. Spectra are drawn with vertical offsets for clarity.

intensity is detected near the fiber tips (figure 10(b)). The emission intensity increases continuously as the position approaches the tips, where the guided light is efficiently outcoupled (figure 10(c)). Assuming linear amplification of spontaneous emission and uniform scattering efficiency across the fiber, the emission intensity profile can be fitted by the

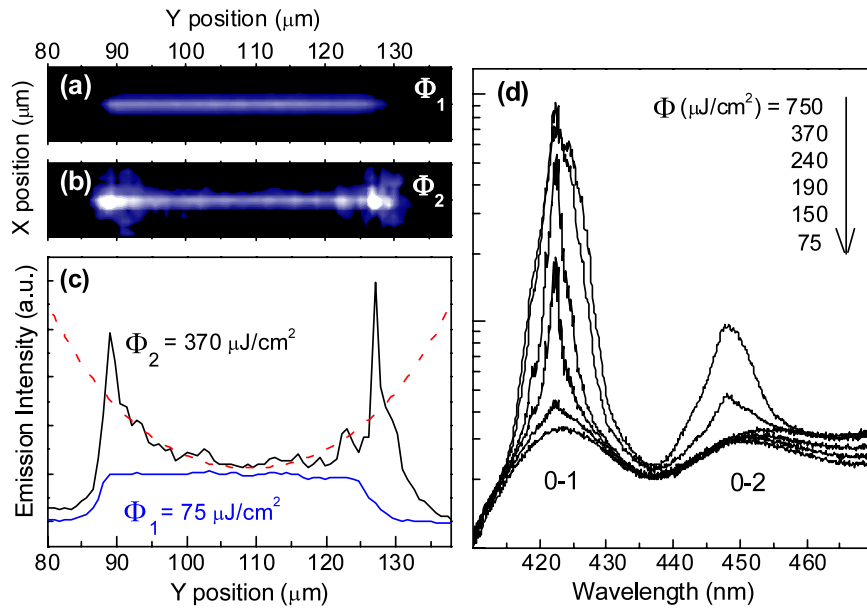


Figure 10. Time integrated emission micrographs of a single nanofiber excited by ultrafast pulses, for pump fluences of $\Phi_1 = 75$ (a) and $\Phi_2 = 370 \mu\text{J cm}^{-2}/\text{pulse}$ (b). Panel (c): time and spectrally integrated spatial profiles of the emission intensity. The dashed line is a fit to the measured emission profile (fluence Φ_2). Panel (d): time integrated emission spectra for different values of the excitation fluence. The spectra are spatially integrated over the nanofiber region. Sample temperature: 300 K.

function $I_T(z) = I(z) + I(L - z)$, where $I(z) \sim [\exp(gz) - 1]/g$; z is the distance from a fiber tip, g the net modal gain coefficient, and L the fiber length.

Occurrence of ASE with negligible coherent feedback is confirmed by the spectral analysis of the emission intensity above the amplification threshold, which shows line narrowing of the emission towards the center of the vibronic bands (figure 10(d)), while spectral fringes relating to a Fabry–Perot resonator $\sim 40 \mu\text{m}$ long are not visible. Curve fitting of intensity profiles yields $g_1 \sim 1200 \text{ cm}^{-1}$ for the 0–1 emission band and $g_2 \sim 700 \text{ cm}^{-1}$ for the 0–2 emission band at the highest excitation fluence of $750 \mu\text{J cm}^{-2}/\text{pulse}$. Assuming an excitation density of $\sim 10^{20} \text{ cm}^{-3}$, typical fiber propagation losses of $\sim 300 \text{ cm}^{-1}$ [20] and an optical confinement factor of $\sim 1\%$, one estimates the stimulated emission cross-section of *p*-6P to be $\sim 10^{-15} \text{ cm}^2$ at the 0–1 emission peak. Time-resolved differential transmission measurements yield a smaller value, $\approx 2 \times 10^{-16} \text{ cm}^2$ (see section 6). The overestimation of the cross-section value yielded by the present analysis of the ASE spatial profiles is attributed to the lack of accurate knowledge of the optical confinement factor of gain-guided modes and the optical loss coefficient in singly selected nanofibers.

6. Optical gain performance and nonlinear excited-state dynamics of *p*-6P epitaxial films

The potential of organic films for laser technologies stems from the ability to achieve lasing thresholds compatible with indirect electrical pumping by inexpensive and convenient light sources. Lasing performance results from both extrinsic factors (i.e., optical confinement of lasing modes in the gain medium, propagation and feedback losses) and intrinsic gain

performance of the active medium. The latter is quantified by the figure of merit (FOM) for optical amplification, defined as $\text{FOM} = \sigma_G B_G \tau$, with σ_G being the net-gain cross-section, B_G its bandwidth, and τ the excited-state lifetime at operating excitation intensity. These parameters can be retrieved from analysis of the excited-state dynamics of the system.

We resort to time-resolved fluorescence and pump–probe measurements with ultrafast excitation to study the excited-state dynamics of *p*-6P crystalline nanofiber films. We investigate ensembles of close-packed nanofibers displaying high ASE/lasing thresholds ($> 100 \mu\text{J cm}^{-2}/\text{pulse}$) to ensure that the population dynamics is not perturbed by stimulated emission. Ultrafast excitation experiments are performed using pulses 150 fs long delivered by an optical parametric amplifier pumped by the Ti:sapphire amplified laser with 1 kHz repetition rate. The sample emission is spectrally dispersed in a single spectrometer and temporally resolved with a visible streak camera having a temporal resolution of $\sim 20 \text{ ps}$ [26]. A continuous-flow, low-vibration cold-finger cryostat fed with liquid air is used to vary the sample temperature in the 80–300 K range. Complementary differential transmission ($\Delta T/T$) measurements are performed using broadband pulses, obtained by supercontinuum generation on a sapphire plate, as the optical probe. Pump–probe time delay is controlled by a motorized optical delay stage [31].

6.1. Time-resolved fluorescence studies

The results of time-resolved fluorescence studies are summarized in figure 11, where the fluorescence decay rate constant is reported as a function of excitation fluence. A series of fluorescence decay traces taken at 80 K is shown in the inset of figure 11. It is clear that at high pump fluences the

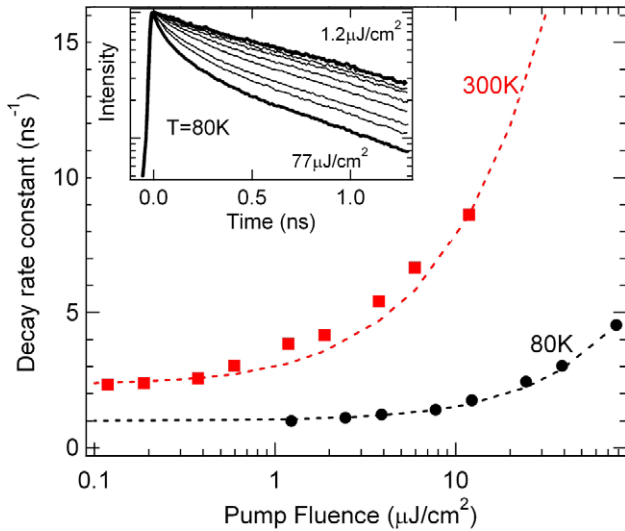


Figure 11. Characteristic inverse decay times of the optical emission intensity of *p*-6P nanofibers excited by ultrafast pulses at 380 nm. Lattice temperature: 300 K (red squares); 80 K (black circles). Dashed lines: model simulations of singlet exciton decay dynamics with account taken of monomolecular and bimolecular recombination processes. Parameter values: $k_0 = 1 \times 10^9 (2.3 \times 10^9) \text{ s}^{-1}$, $\kappa_{SS} = 3 \times 10^{-9} (4 \times 10^{-8}) \text{ cm}^3 \text{ s}^{-1}$ for $T = 80 (300) \text{ K}$. Inset: fluorescence decay traces measured at 80 K for excitation fluences of 1.2, 2.5, 3.9, 7.8, 12, 25, 39, and $77 \mu\text{J cm}^{-2}/\text{pulse}$.

excited-state decay dynamics is dominated by nonradiative, density-dependent processes which are ascribed to singlet–singlet (bimolecular) annihilations [26, 32, 33].

Bimolecular recombination strongly depends on the lattice temperature. Upon fitting the initial 1/e decay times with the results of model simulations of the decay dynamics, we estimate that the bimolecular coefficient (κ_{SS}) increases from 3×10^{-9} to $4 \times 10^{-8} \text{ cm}^3 \text{ s}^{-1}$ when the lattice temperature is increased from 80 to 300 K. The linear (monomolecular) recombination rate constant (k_0) also exhibits a temperature dependence, increasing from 1×10^9 to $2.3 \times 10^9 \text{ s}^{-1}$ for the same temperature raise. At 80 K, bimolecular processes kick in for pump fluences of $\sim 2\text{--}4 \mu\text{J cm}^{-2}$, while at room temperature the linear recombination regime holds only up to excitation fluences on the order of $0.1 \mu\text{J cm}^{-2}$, well below the lowest values reported for the lasing threshold in nanofibers excited by subpicosecond pulses.

The temperature dependence of bimolecular processes indicates that exciton migration is a thermally activated process [34]. Activation energy is possibly related to the presence of energetic disorder in *p*-6P nanostructured films [35].

6.2. Ultrafast pump–probe studies

Stimulated emission (SE) and photoinduced absorption (PA) are studied using spectrally resolved differential transmission measurements as a function of the pump–probe time delay (Δt). Transmission spectra taken for various pump–probe delays are shown in figure 12. At short delays ($\Delta t = 1 \text{ ps}$), the system response is characterized by broadband SE

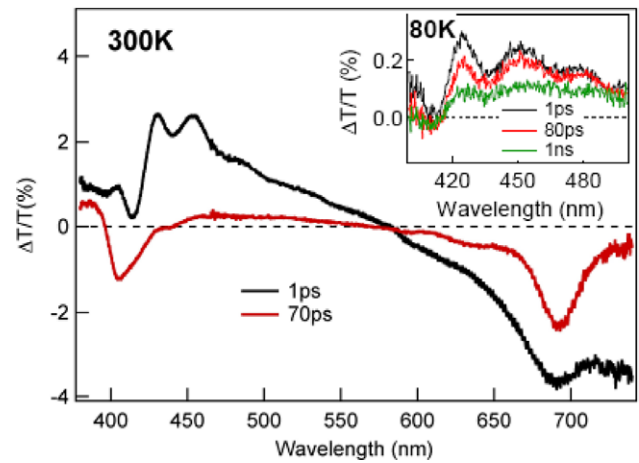


Figure 12. Differential transmission spectra of a *p*-6P nanofiber film excited by ultrafast pulses at 360 nm, for different lattice temperatures and pump–probe delays. Main panel (inset): pump fluence of $90 (10) \mu\text{J cm}^{-2}/\text{pulse}$ and lattice temperature of 300 (80) K.

extending from the deep blue to the orange ($B_G \sim 1 \text{ eV}$) and exhibiting the vibronic progression of singlet excitons in *p*-6P crystalline nanofibers. The SE cross-section is found to be $\approx 2 \times 10^{-16} \text{ cm}^2$, as estimated from the $\Delta T/T$ signal amplitude (at $\Delta t = 0$) at the 0–2 vibronic peak, assuming that primary photoexcitations are singlet excitons. On the long wavelength side, SE of singlet excitons turns into PA of triplet excitons and polarons created on ultrafast timescales [36].

At room temperature and high pump fluences ($\sim 90 \mu\text{J cm}^{-2}$), broadband SE decays rapidly due to singlet–singlet annihilations and a PA band arises in a complementary way at short wavelengths, near the optical gap of the material. This PA band is relatively long lived (its decay time being longer than 1 ns) and is attributed to intermolecular, charge-transfer excitons generated through singlet–singlet annihilations [37]. At cryogenic temperatures (80 K) and lower excitation fluences ($\sim 10 \mu\text{J cm}^{-2}$), bimolecular recombination is strongly suppressed: the excited-state lifetime (τ) increases up to $\sim 1 \text{ ns}$ and the PA band associated with secondary charge-transfer excitons disappears (inset of figure 12).

Overall, it is concluded that excited-state lifetime shortening emerges as a primary effect of singlet–singlet annihilations. As a secondary effect, a (nonlinear) population of intermolecular excitons is promoted, whose absorption spectrum overlaps with the gain spectrum of emissive (singlet) excitons. Combined effects of lifetime shortening, net-gain reduction and bandwidth shrinking caused by photoinduced absorption are detrimental to lasing action in nanofibers excited by long (nanosecond) pulses.

Sample cooling to cryogenic temperatures makes it possible to circumvent fast bimolecular decay and photoinduced absorption and reach best optical gain performance, with $\sigma_G \sim 2 \times 10^{-16} \text{ cm}^2$, $B_G \sim 1 \text{ eV}$ and $\tau \sim 1 \text{ ns}$. Direct demonstration of the occurrence of *monomolecular lasing* (i.e., lasing in the linear recombination regime) at cryogenic temperatures is provided in figure 13, which displays the time–wavelength spectrogram of the emission intensity of nanofibers excited by

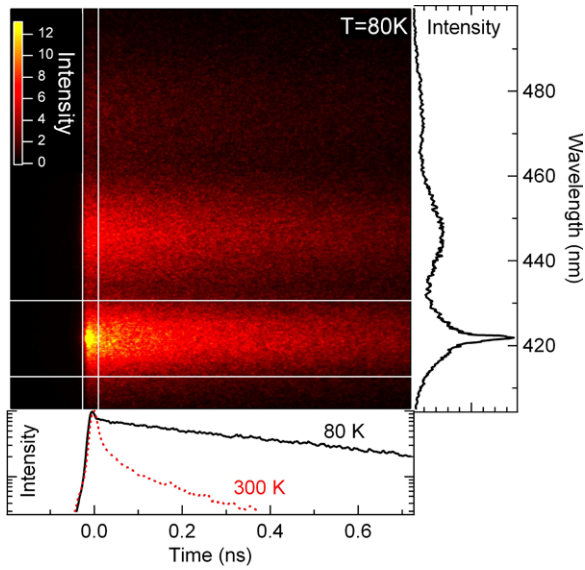


Figure 13. False-color image of the temporally and spectrally resolved emission intensity of nanofibers excited by subpicosecond pulses at 360 nm. Sample temperature: 80 K; excitation fluence: $7 \mu\text{J cm}^{-2}$ /pulse. Vertical (horizontal) white lines delimit the area for temporal (spectral) integration. Right panel: emission spectrum, integrated in the first 30 ps after excitation pulse arrival. Bottom panel: emission decay traces integrated over the 0–1 vibronic band of *p*-6P. The solid (dashed) line is the time profile at 80 (300) K.

subpicosecond pulses. The spectral profile (right panel) shows evidence of lasing emission on top of the 0–1 spontaneous emission band. The time profile analysis (bottom panel) demonstrates that at 80 K prompt laser emission leaves the system with a population of singlet excitons that undergoes monomolecular recombination with ~ 1 ns decay time.

6.3. Nanofiber lasing with nanosecond-pulsed excitation: experiment and theory

To assess lasing performance of *p*-6P nanofibers under practical pumping conditions, we investigate lasing action with pulses 4 ns long at 355 nm as the excitation source. The pulses are delivered by an optical parametric oscillator pumped by a Q-switched neodymium-doped yttrium aluminum garnet (Nd:YAG) laser with 10 Hz repetition rate. The emission is sent through a single spectrometer and acquired by an image-intensified, time-gateable CCD camera with ~ 3 ns temporal resolution. We study a nanofiber ensemble exhibiting a low lasing threshold of $\sim 6 \mu\text{J cm}^{-2}$ /pulse under ultrafast pumping [26].

At 80 K, the lasing threshold occurs at a pump intensity (I_{th}) of $\sim 15 \text{ kW}_p \text{ cm}^{-2}$. Assuming that the system is in a monomolecular regime, the equivalent lasing threshold under ultrafast pumping ($\Phi_{\text{th,eq}}$) is close to the experimental one ($\Phi_{\text{th,eq}} = I_{\text{th}}/k_0 \approx 10 \mu\text{J cm}^{-2}$ /pulse). Thus, at cryogenic temperatures nanosecond lasing performance is found not to be affected by PA of secondary excitations. When the temperature is raised from 80 to 300 K, a 50-fold increase in lasing threshold is observed, from 16 to $\sim 800 \text{ kW}_p \text{ cm}^{-2}$. This dramatic increase in threshold intensity cannot be explained

with just lifetime shortening due to bimolecular effects, and demonstrates the importance of PA at room temperature.

Numerical simulations of the nanofiber laser dynamics are carried out to quantify the effects of optical and population losses. A rate-equation model is developed for the coupled densities of singlet excitons (N_S), charge-transfer excitons (N_{CT}) and photons (N_P). In the single-mode approximation for the laser resonator, the model equations are

$$\frac{dN_S}{dt} = G(t) + k_{\text{CT}}N_{\text{CT}} - k_0N_S - \frac{1}{2}\kappa_{\text{SS}}N_S^2 - \sigma_{\text{SE}}vN_PN_S$$

$$\frac{dN_{\text{CT}}}{dt} = \frac{1}{4}\kappa_{\text{SS}}N_S - k_{\text{CT}}N_{\text{CT}} - \sigma_{\text{PA}}vN_PN_{\text{CT}}$$

$$\frac{dN_P}{dt} = \epsilon k_R N_S + \sigma_{\text{SE}}vN_PN_S - \sigma_{\text{PA}}vN_PN_{\text{CT}} - k_L N_P$$

where $G(t)$ is the time-dependent pump rate, k_{CT} the decay rate constant of charge-transfer excitons, $\sigma_{\text{SE(PA)}}$ the stimulated emission (photoinduced absorption) cross-section of singlet (charge-transfer) excitons, v the speed of light in the medium, k_R the radiative emission rate constant of singlet excitons, ϵ the fraction of spontaneous emission captured into the lasing mode, and k_L the linear optical loss constant of the lasing mode. The parameter values are as follows: $\epsilon = 10^{-4}$, $k_R = 0.7 \times 10^9 \text{ s}^{-1}$ ($k_R/k_0 \sim 0.3$), $\sigma_{\text{SE}} = 2 \times 10^{-16} \text{ cm}^2$, $\sigma_{\text{PA}} = 1 \times 10^{-17} \text{ cm}^2$ (the ratio $\sigma_{\text{PA}}/\sigma_{\text{SE}}$ is consistent with differential transmission measurements). The temperature-dependent values of the singlet exciton recombination constants (k_0 , κ_{SS}) are the experimental ones. Charge-transfer excitons are assumed to recombine into singlet excitons with $k_{\text{CT}} = 1 \text{ ns}^{-1}$. Gaussian-shaped pump pulses 4 ns long have 100% efficiency of conversion into singlet excitons; the singlet exciton generation rate is thus given by $G(t) = I(t)/(E_p d)$, $I(t)$ being the pump intensity profile, E_p the pump photon energy and d the film thickness.

In figure 14, the calculated lasing threshold is plotted against the loss coefficient ($\alpha_L = k_L/v$) of the fiber resonator, which includes both internal linear losses and feedback losses. At small values of α_L , lasing is achieved in the monomolecular regime and the lasing threshold increases linearly with α_L . For high enough α_L values, bimolecular recombinations become important and the lasing threshold starts growing superlinearly with α_L . The superlinear behavior becomes very sensitive to temperature once PA by charge-transfer excitons is turned on (solid curves).

Calculated thresholds are consistent with experimental ones assuming that the nanofibers investigated have an average resonator loss coefficient of about 200 cm^{-1} . From the results of model calculations, we conclude that loss values as small as 10 cm^{-1} are necessary to lower the lasing threshold with nanosecond-pulsed excitation to values $< 1 \text{ kW}_p \text{ cm}^{-2}$ that are compatible with indirect pumping by compact nanosecond lasers. A few strategies are envisaged for achieving *p*-6P nanofiber lasing in the monomolecular regime at room temperature. Doping the *p*-6P crystals with acceptor molecules emitting at longer wavelengths could be a viable route to hampering exciton migration and hence exciton–exciton annihilations. Crystal doping would also minimize reabsorption losses. Alternatively, *p*-6P crystalline films could

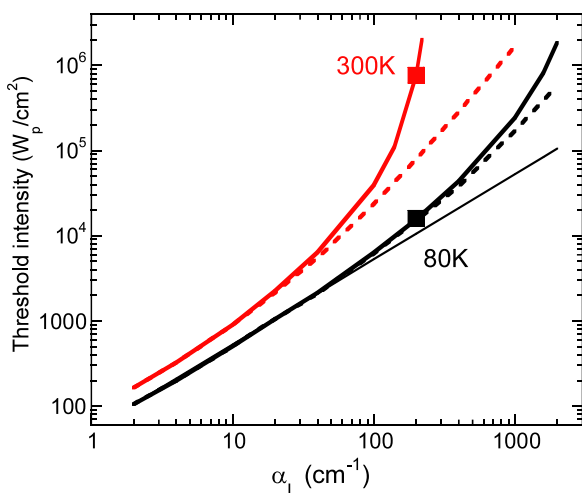


Figure 14. Calculated lasing threshold intensity of a *p*-6P nanofiber versus the loss coefficient (α_L) of the fiber resonator. Pulsed excitation with pulses 4 ns long is assumed. Continuous lines: bimolecular recombination and photoinduced absorption are both included in the calculations. Dashed lines: photoinduced absorption is turned off. Black (red) lines refer to 80 (300) K. The thin straight line highlights the lasing response of the same nanofiber in the absence of bimolecular recombination (at 80 K). Solid squares are the experimental data obtained with nanosecond-pulsed excitation.

be integrated in distributed feedback structures to decrease feedback losses. Grating structures printed on suitable polymer coatings by nanoimprint techniques [12] could serve as cost-effective solutions.

7. Organic epitaxial nanofibers for photonic sensing

Low-threshold random lasing can be exploited to achieve high photonic sensitivity to various agents. Miniaturized random laser sources have been envisaged to enable new functionalities for next-generation information technologies [3, 38].

On the basis of model simulations of the coherent optical response of a random medium, we estimate that a typical *p*-6P epitaxial nanofiber with a length of $\sim 100 \mu\text{m}$ and a dozen thin ($\sim 200 \text{ nm}$) breaks would display *attoliter* sensitivity in detecting small volumes of index matching fluids (see figure 15(a)). Also, strain sensors with very large ($> 10^3$) gauge factor and high dynamic range could be obtained by optical interrogation of single nanofibers aligned parallel to the strain axis (figures 15(b) and (c)).

We add that surface adsorption of molecular species in nanofibers assembled from suitably functionalized oligomers [39] could generate photonic chemosensing, e.g., by modulation of the effective refractive index of the nanofiber resonance modes. Photonic sensitivity could be further enhanced near the lasing threshold, as recently demonstrated in detecting ultralow molecular traces using an organic distributed feedback laser [40].

8. Summary

We presented experimental data on coherent and incoherent random lasing in *para*-sexiphenyl epitaxial nanofibers grown

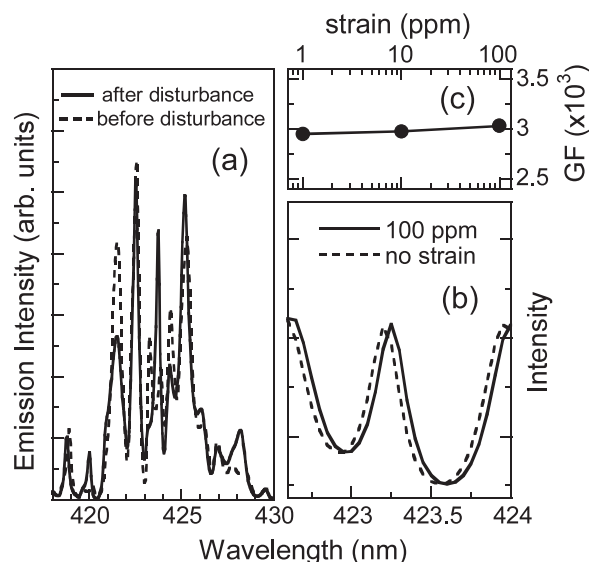


Figure 15. Model calculations of the photonic sensitivity of a one-dimensional random medium such as a *p*-6P epitaxial nanofiber. (a) Coherent emission spectrum before and after optical neutralization of a fiber break upon air gap filling with index matching fluid. (b) Resonance wavelength shift in response to a 100 ppm axial strain. (c) Strain gauge factor as a function of the strain strength. The gauge factor (GF) is defined from the relation $\Delta I/I (\text{ppm}) = \text{GF} \cdot \text{strain} (\text{ppm})$, where I is the optical emission intensity.

on muscovite mica. One-dimensional random lasing and linear optical amplification are demonstrated in individual nanofibers. Model calculations of coherent light propagation in one-dimensional random media are in agreement with experimental observations. Nonlinear excited-state losses, i.e., the bimolecular recombination and photoinduced absorption, are measured by ultrafast spectroscopy techniques, and their impact on random lasing performance under nanosecond-pulsed pumping is determined. Model calculations of the nanofiber laser dynamics are able to reproduce lasing thresholds measured under nanosecond pumping. Lastly, potential applications of organic epitaxial nanofibers in photonic sensing are discussed.

Acknowledgments

We acknowledge the scientific collaboration of F Cordella, M Saba, R Orrù, J E Communal, P Verzeroli, M Marceddu, A Anedda, A Andreev, G Hlawacek, C Teichert, H Sitter, N S Sariciftci, F Balzer, V G Bordo, S B Petersen, M T Neves-Petersen, K Thilsing-Hansen, H-G Rubahn, A Mura, and G Bongiovanni. We also thank G Del Fiacco for technical assistance.

References

- [1] Cao H 2003 *Waves Random Media* **13** R1
Cao H 2005 *J. Phys. A: Math. Gen.* **38** 10497
- [2] Cao H, Xu J Y, Zhang D Z, Chang S-H, Ho S T, Seelig E W, Liu X and Chang R P H 2000 *Phys. Rev. Lett.* **84** 5584

- Wiersma D S, Bartolini P, Lagendijk A and Righini R 1997 *Nature* **390** 671
- [3] Wiersma D S 2000 *Nature* **406** 132
- [4] Polson R C and Vardeny Z V 2004 *Appl. Phys. Lett.* **85** 1289
- [5] Samuel I D W and Turnbull G A 2007 *Chem. Rev.* **107** 1272
- [6] McGehee M D and Heeger A J 2000 *Adv. Mater.* **12** 1655
- [7] Frolov S V, Vardeny Z V, Yoshino K, Zakhidov A and Baughman R H 1999 *Phys. Rev. B* **59** R5284
- [8] Anni M, Lattante S, Cingolani R, Gigli G, Barbarella G and Favaretto L 2003 *Appl. Phys. Lett.* **83** 2754
- Anni M, Lattante S, Stomeo T, Cingolani R, Gigli G, Barbarella G and Favaretto L 2004 *Phys. Rev. B* **70** 195216
- [9] Quochi F, Cordella F, Mura A, Bongiovanni G, Balzer F and Rubahn H-G 2005 *J. Phys. Chem. B* **109** 21690
- [10] Zhao Y S, Peng A, Fu H, Ma Y and Yao J 2008 *Adv. Mater.* **20** 1661
- [11] O'Carroll D, Lieberwirth I and Redmond G 2007 *Nat. Nanotechnol.* **2** 180
- [12] Camposeo A, Di Benedetto F, Stabile R, Neves A A R, Cingolani R and Pisignano D 2009 *Small* **5** 562
- Di Benedetto F, Camposeo A, Pagliara S, Mele E, Persano L, Stabile R, Cingolani R and Pisignano D 2008 *Nat. Nanotechnol.* **3** 614
- [13] Yanagi H and Morikawa T 1999 *Appl. Phys. Lett.* **75** 187
- [14] Andreev A, Matt G, Brabec C J, Sitter H, Badt D, Seyringer H and Sariciftci N S 2000 *Adv. Mater.* **12** 629
- [15] Balzer F and Rubahn H-G 2001 *Appl. Phys. Lett.* **79** 3860
- [16] Andreev A, Quochi F, Cordella F, Mura A, Bongiovanni G, Sitter H, Hlawacek G, Teichert C and Sariciftci N S 2006 *J. Appl. Phys.* **99** 034305
- [17] Plank H, Resel R, Sitter H, Andreev A, Sariciftci N S, Hlawacek G, Teichert C, Thierry A and Lotz B 2003 *Thin Solid Films* **443** 108
- Teichert C, Hlawacek G, Andreev A, Sitter H and Sariciftci N S 2005 *Appl. Phys. A* **82** 665
- [18] Kjelstrup-Hansen J, Henrichsen H H, Bøggild P and Rubahn H-G 2006 *Thin Solid Films* **515** 827
- [19] Birendra-Singh T, Hernandez-Sosa G, Neugebauer H, Andreev A, Sitter H and Sariciftci N S 2006 *Phys. Status Solidi b* **243** 3329
- [20] Balzer F, Bordo V G, Simonsen A C and Rubahn H-G 2003 *Phys. Rev. B* **67** 115408
- [21] Volkov V S, Bozhevolnyi S I, Bordo V G and Rubahn H-G 2004 *J. Microsc.* **215** 241
- [22] Yanagi H and Yoshiki A 2004 *Appl. Phys. Lett.* **84** 4783
- [23] Yanagi H, Ohara T and Morikawa T 2001 *Adv. Mater.* **13** 1452
- [24] Quochi F, Cordella F, Mura A, Bongiovanni G, Balzer F and Rubahn H-G 2006 *Appl. Phys. Lett.* **88** 041106
- [25] Quochi F, Cordella F, Orrù R, Communal J E, Verzeroli P, Mura A, Bongiovanni G, Andreev A, Sitter H and Sariciftci N S 2004 *Appl. Phys. Lett.* **84** 4454
- [26] Quochi F *et al* 2008 *Adv. Mater.* **20** 3017
- [27] Balzer F, Beermann J, Bozhevolnyi S I, Simonsen A C and Rubahn H-G 2003 *Nano Lett.* **3** 1311
- [28] Plank H, Resel R, Purger S, Keckes J, Thierry A, Lotz B, Andreev A, Sariciftci N S and Sitter H 2001 *Phys. Rev. B* **64** 235423
- [29] Andreev A, Sitter H, Brabec C J, Hinterdorfer P, Springholz G and Sariciftci N S 2001 *Synth. Met.* **121** 1379
- [30] Burin A L, Ratner M A, Cao H and Chang R P H 2001 *Phys. Rev. Lett.* **87** 215503
- [31] Cordella F, Quochi F, Saba M, Andreev A, Sitter H, Sariciftci N S, Mura A and Bongiovanni G 2007 *Adv. Mater.* **19** 2252
- [32] Pope M and Swenberg C E 1999 *Electronic Processes in Organic Crystals and Polymers* (New York: Oxford University Press)
- [33] Baldo M A, Holmes R J and Forrest S R 2002 *Phys. Rev. B* **66** 035321
- [34] Wiesenhofer H, Zojer E, List E J W, Scherf U, Brédas J-L and Beljonne D 2006 *Adv. Mater.* **18** 310
- [35] Kadamchuk A, Andreev A, Sitter H, Sariciftci N S, Skryshevsky Y, Piryatinski Y, Blonsky I and Meissner D 2004 *Adv. Funct. Mater.* **14** 970
- [36] Zenz C, Cerullo G, Lanzani G, Graupner W, Meghdadi F, Leising G and De Silvestri S 1999 *Phys. Rev. B* **59** 14336
- [37] Cerullo C, Lanzani G, De Silvestri S, Egelhaaf H-J, Luer L and Oelkrug D 2000 *Phys. Rev. B* **62** 2429
- [38] Wiersma D S and Cavalieri S 2001 *Nature* **414** 708
- [39] Schiek M, Lützen A, Koch R, Al-Shamery K, Balzer F, Frese R and Rubahn H-G 2005 *Appl. Phys. Lett.* **86** 153107
- [40] Rose A, Zhu Z, Madigan C F, Swager T M and Bulović V 2005 *Nature* **434** 876